Supporting Information

In situ self-reconstructed hierarchical bimetallic oxyhydroxide nanosheets of metallic sulfides for high-efficiency electrochemical water splitting

Yaning Fan[a], Junjun Zhang[a]*, Jie Han[b]*, Mengyuan Zhang[c], Weiwei Bao[b], Hui Su[d], Nailiang Wang[a], Pengfei Zhang[a,c*], Zhenghong Luo[a,c]

[a]State Key Laboratory of High-Efficiency Utilization of Coal and Green Chemical Engineering. College of Chemistry and Chemical Engineering, Ningxia University, Yinchuan, Ningxia, 750021, China. E-mail: zhangjj089@nxu.edu.cn; pfzhang@nxu.edu.cn.

[b]National & Local Joint Engineering Laboratory for Slag Comprehensive Utilization and Environmental Technology, School of Material Science and Engineering, Shaanxi University of Technology, Hanzhong, Shaanxi, 723000 P. R. China E-mail:

[c]School of Chemistry and Chemical Engineering, Shanghai Jiao Tong University, Shanghai, 200240, P. R. China. E-mail: chemistryzpf@sjtu.edu.cn

[d]Department of Chemistry, FRQNT Centre for Green Chemistry and Catalysis, McGill University, 801 Sherbrooke Street W., Montreal, QC H3A 0B8, Canada

*Corresponding author.
** State Key Laboratory of High-Efficiency Utilization of Coal and Green Chemical Engineering. College of Chemistry and Chemical Engineering, Ningxia University, Yinchuan, Ningxia, 750021,

E-mail addresses: zhangjj089@nxu.edu.cn (J. J. Zhang); pfzhang@nxu.edu.cn (P.F. Zhang); hanjie@snut.edu.cn (J. Han)

1. Experiment Section

1.1 Materials

$Fe(NO_3)_3·9H_2O$ (Aladdin, ≥ 99.9%), $Co(NO_3)_3·6H_2O$(Aladdin, ≥ 99.9%), thiourea (Aladdin, ≥99.0%), IrO_2 (Macklin, Ir ≥ 84.5%), Pt/C（Adamas-beta, Pt ≥ 20%), glycol (Aladdin, Ltd. analytically pure), Nafion dispersion, anhydrous ethanol (99.9%), hydrochloric acid (37%), acetone, deionized water. All chemicals were utilized in their original state without undergoing additional purification.

1.2 Substrate preparation

Cut the purchased Nickel-iron foam(NIF) into 1cm*3cm rectangular pieces and place them in a prepared 3mol/L hydrochloric acid solution. Ultrasonically clean for 20-30 minutes. After the ultrasonic cleaning is complete, wash the NIF several times with water and anhydrous ethanol until the solution reaches a pH of around 7. Then, quickly absorb any remaining anhydrous ethanol and water on the surface of the cleaned NIF using filter paper.

1.3 Preparation of S-$FeCo_{x:y}$/NIF.

Measuring 3 mmol of $Fe(NO_3)_3·9H_2O$ and $Co(NO_3)_2·6H_2O$ in a 1:2, 1:1, 2:1 Fe: Co molar ratio, and dissolving them with 10 mmol of thiourea in 50 mL of ethylene glycol based on the specified feed ratios. Following ultrasonic dissolution, the solution underwent vigorous stirring until it achieved clarity and transparency. The impeccably cleaned NIF was promptly immersed in a 100 mL polytetrafluoroethylene-lined high-pressure hydrothermal reactor, along with the solution, maintained at 180°C for 12 hours. After naturally cooling to room temperature, the electrode plates underwent multiple washes with water and ethanol. The resulting sample powder underwent centrifugation and was alternatively washed with water and ethanol thrice, followed by overnight drying at 60°C.

1.4 Preparation of S-Co/NIF and S-Fe/NIF.

When preparing S-Co, 3mmol of $Co(NO_3)_2·6H_2O$ and 10mmol of thiourea were weighed, and 3mmol of $Fe(NO_3)_3·9H_2O$ and 10mmol of thiourea were weighed when preparing S-Fe. The other steps were consistent with 1.3.

1.5 IrO_2 and Pt/C electrode preparation

10.0 mg Pt/C and IrO_2 were added into a 1.5ml centrifuge tube, and 600uL deionized water, 400uL dehydrated alcohol, and 10uL Nafion dispersion were added with a pipette gun, and ultrasound for 60 min. The prepared ink was applied to INF (1*1cm^2) with a pipette at 46 uL each time, and dried for 15 min after each application, for a total of 4 times, followed by 2h drying at 60°C.

1.6 Electrochemical characterizations

Electrochemical performance tests were performed at room temperature using an electrochemical workstation (DH7000C, Donghua, Jiangsu, China). $FeCo_{1:1}$/NIF, S-$FeCo_{1:2}$/NIF, S-$FeCo_{2:1}$/NIF, S-Fe/NIF, S-Co/NIF, and NIF as working electrode, graphite rod, and standard Hg/HgO electrode as counter electrode and reference electrode, 1.0 M KOH as electrolyte.

At the initiation of the OER experiment, the catalyst underwent 20 cycles of CV at a scan rate of 10 mV/s within the voltage range of 0.5-1.2V to achieve stabilization of the catalyst surface. The catalyst's oxygen evolution performance was assessed through LSV within the 0-1.2V vs.Hg/HgO range. C_{dl} measurements were conducted by altering scan rates (20, 40, 60, 80, 100 mV/s) in a potential window nearly devoid of a Faradaic process. The EIS test encompassed a frequency range of 0.1-10000Hz, with in-situ impedance measurements conducted using EIS within the 0.45-0.80V range. Subsequently, 2000 CV cycles were executed at 50 mV/s within the 0.5-1.2 V range. Catalyst stability was assessed by comparing LSV and EIS before and after the 2000 CV cycles. The long-term stability was examined at 200 mA cm^{-2}, and concurrently, multi-step currents (100, 200, 300, 400, and 500 mA cm^{-2}) were employed to appraise the catalyst's stability under dynamic current conditions.

At the commencement of the HER experiment, the catalyst was subjected to 20 cycles of CV of 10 mV/s within the -1.3 to -1.9V range to stabilize the catalyst surface. The HER performance was ascertained through LSV within the range of -0.7 to -1.9V vs. Hg/HgO. The EIS test covered a frequency range of 0.1-1000Hz at -1.1V vs. RHE. Within the range of -1.3 to -1.9 V, 2000 CV cycles were conducted of 50 mV s^{-1}. The stability of the catalyst was evaluated by comparing LSV and EIS before and after the 2000 CV cycles. The long-term stability was examined at -100 mA cm^{-2}.

The conditions for industrial water electrolysis involved a 6.0 M KOH solution at 60℃, utilizing S-$FeCo_{1:1}$/NIF as the working electrode in a two-electrode system at 1-2V. The stability was tested at current densities of 100 mA cm^{-2} and 500 mA cm^{-2}.

1.7 Material characterizations

The X-ray diffraction (XRD) patterns were recorded using a Rigaku MiniFlex 600-C X-ray diffractometer equipped with Cu-Kα radiation and operated at a scan rate of 5° min^{-1}. Scanning electron microscopy (SEM) characterizations were performed using a JSM-7800F microscope manufactured by JEOL. Transmission electron microscopy (TEM) and high-resolution transmission electron microscopy (HRTEM) measurements were conducted utilizing a JEOL JEM-F200 microscope. X-ray photoelectron spectroscopy (XPS) measurements were carried out employing a Kratos Axis Ultra DLD spectrometer. Inductively Coupled Plasma (ICP) analysis was performed with the Inductively Coupled Plasma Atomic Emission Spectrometer (iCap7400).

1.8 In-situ Raman measurements

Raman measurements were conducted employing a Raman JY HR800 Spectrometer within the wavenumber range of 200-1000 cm^{-1}. A 50× long working distance objective (8 mm) was utilized, and the excitation laser, with a wavelength of 532 nm, originated from a He-Ne laser with an approximate power of 6 mW. Calibration of the Raman frequency was achieved using a Si wafer. Data acquisition involved Raman readings at various constant potentials (1.15-1.6V vs. RHE), with a stabilization period of 20 seconds preceding each measurement. The catalyst was applied onto hydrophilic carbon paper serving as the working electrode, while the counter electrode and reference electrode for Raman measurement comprised a carbon rod and Hg/HgO, respectively. 1 M KOH electrolyte solution was utilized.

1.9 Computational details

We utilized density functional theory (DFT) to clarify the reaction mechanism. The computations employed the generalized gradient approximation (GGA) with the Periodic Boundary Embedding (PBE) functional, encompassing long-range van der Waals interactions via the DFT-D3 method. The energy cutoff was established at 450

eV, and a 3×3×1 k-point grid was applied. Hubbard-U corrections were incorporated to address the robust correlation of Co's d-electrons, utilizing a U parameter derived from reference (3.52 eV) [1]. Spin polarization was taken into account in the calculation process. To prevent interactions between periodic images, a 15 Å vacuum layer was introduced along the z-direction during structure construction. Convergence criteria for both electronic and ionic optimizations were set at 10^{-7} eV for energy and 0.05 eV $Å^{-1}$ for forces, ensuring adequate accuracy in the calculations.

2. Supplementary Fig.s:

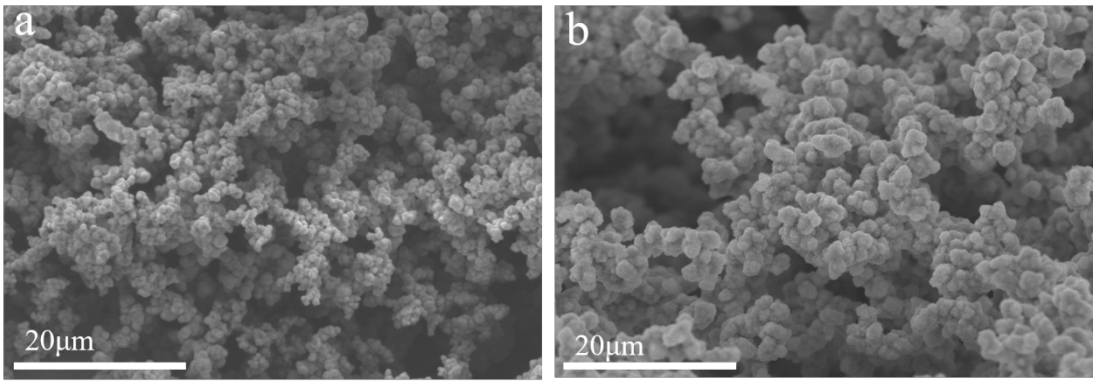

Fig. S1 The SEM image of (a) S-Co/NIF and (b) S-Fe /NIF samples.

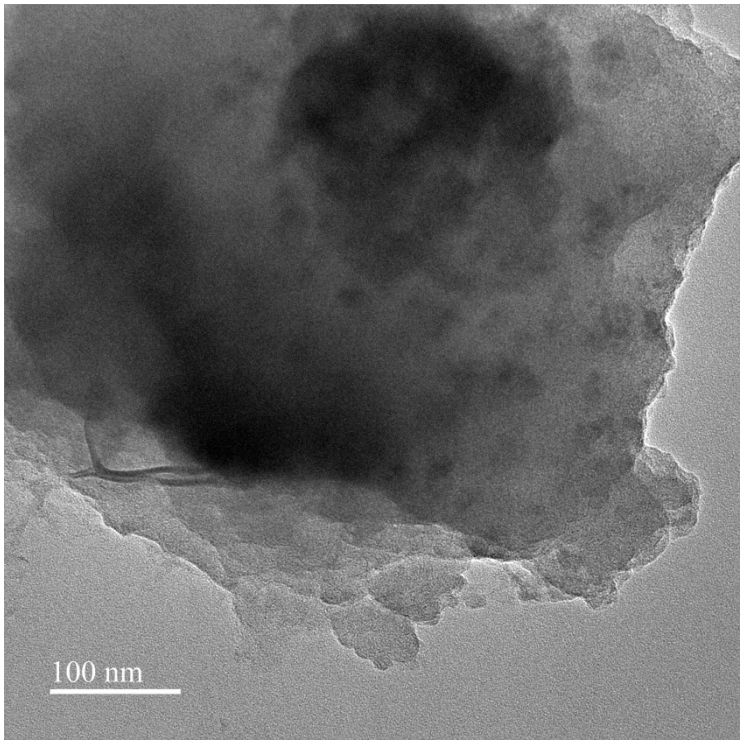

Fig. S2 The TEM image of the S-$FeCo_{1:1}$/NIF sample.

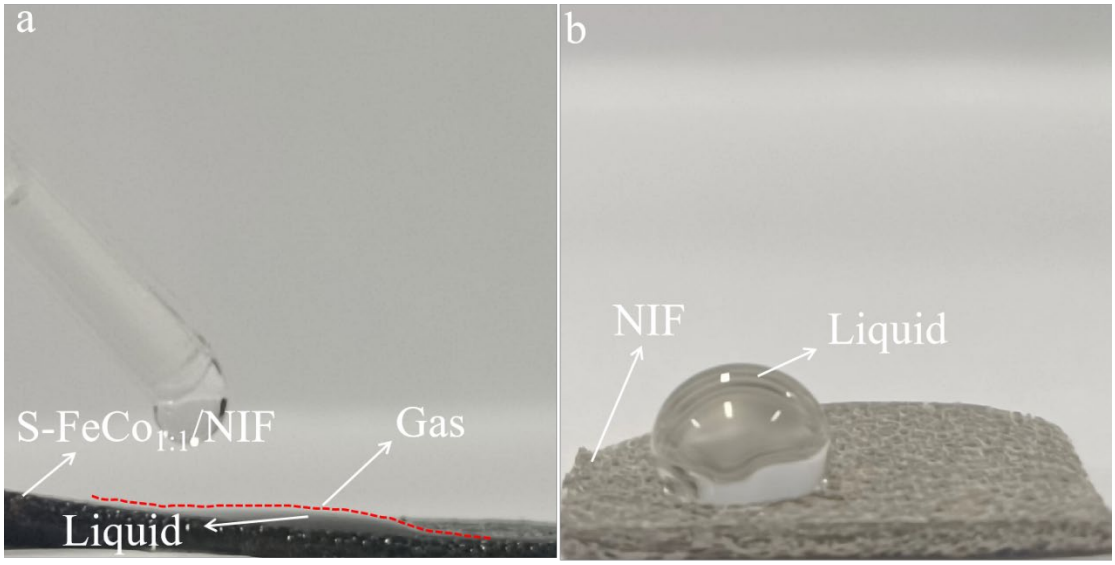

Fig. S3 The (a) S-$FeCo_{1:1}$/NIF and (b) NIF hydrophilicity measurement results.

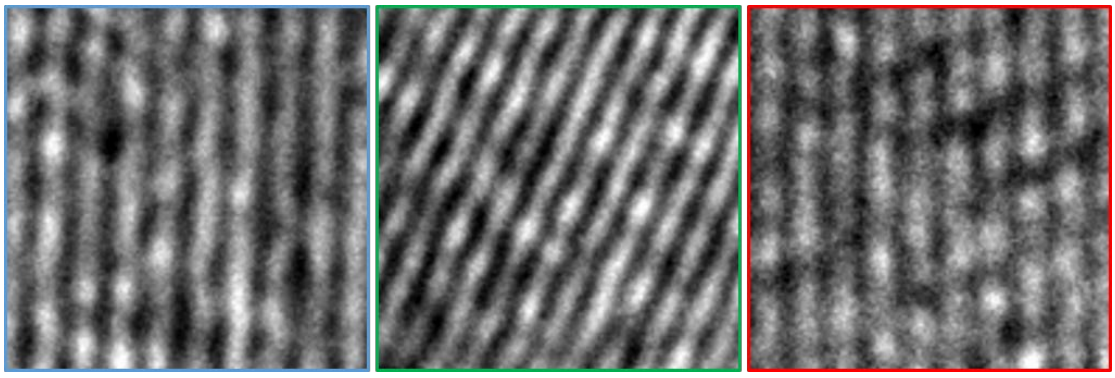

Fig. S4 The inverse fast Fourier transform(IFFT) of S-$FeCo_{1:1}$/NIF sample based on different regions.

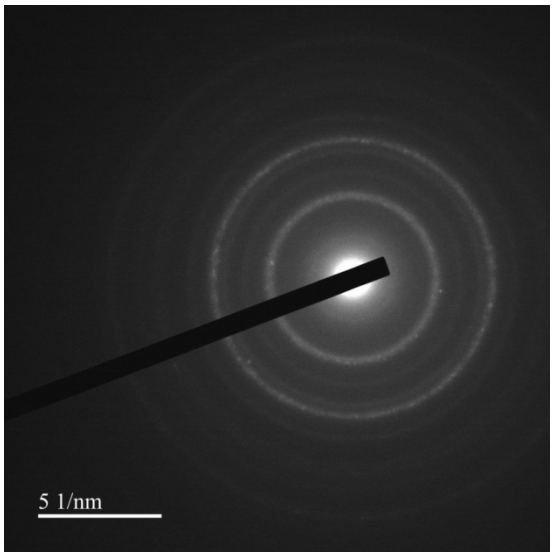

Fig. S5 The SAED image of S-FeCo$_{1:1}$/NIF.

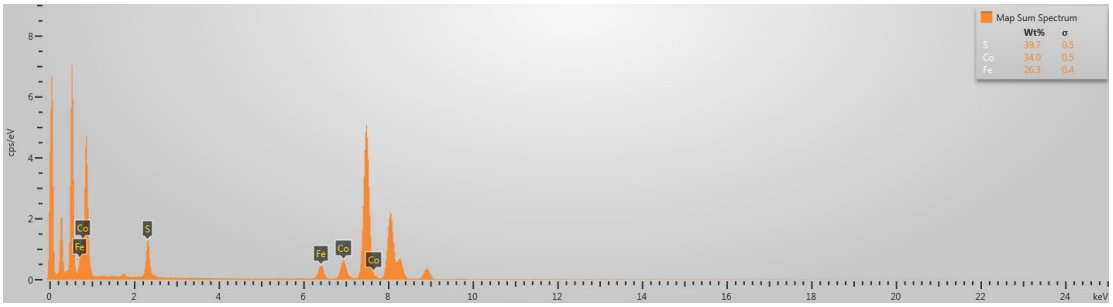

Fig. S6 The EDS of S-FeCo$_{1:1}$/NIF sample.

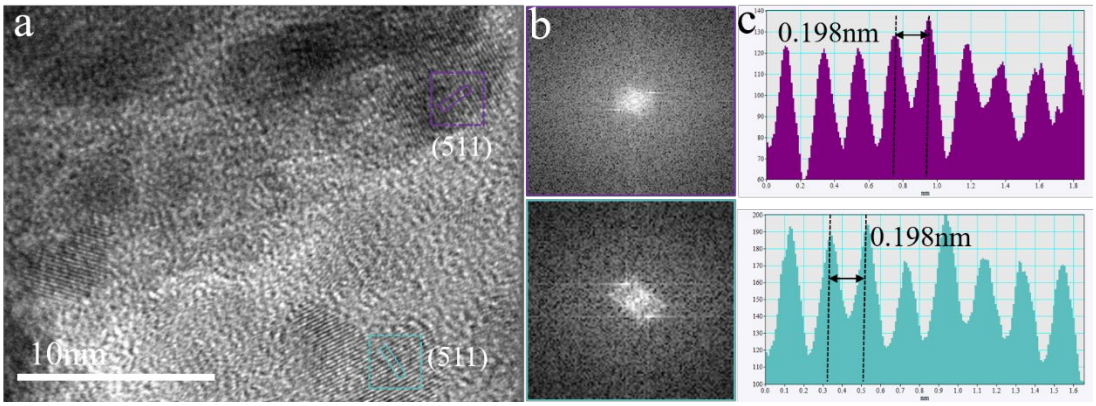

Fig. S7 The (a) HRTEM image, (b) the different regions fast Fourier transform (FFT) and (c) corresponding intensity profiles along with the position of the S-Co/NIF sample.

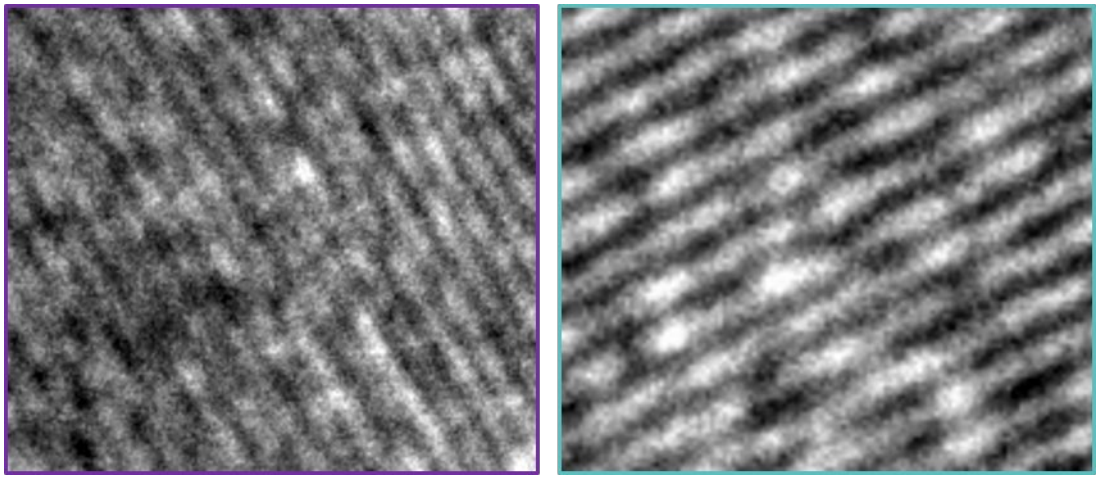

Fig. S8 The inverse fast Fourier transform(IFFT) of S-Co/NIF sample based on different regions.

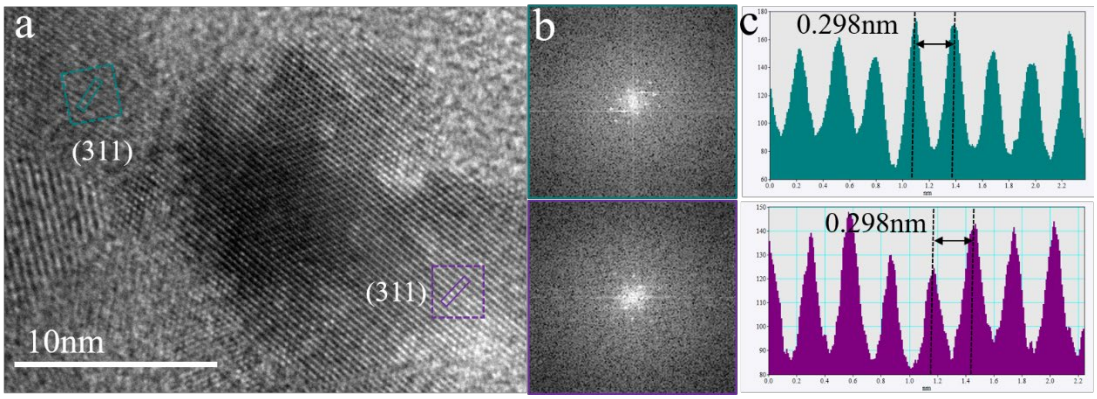

Fig. S9 The (a) HRTEM image, (b) the different regions fast Fourier transform (FFT) and (c) corresponding intensity profiles along with the position of the S-Fe/NIF sample.

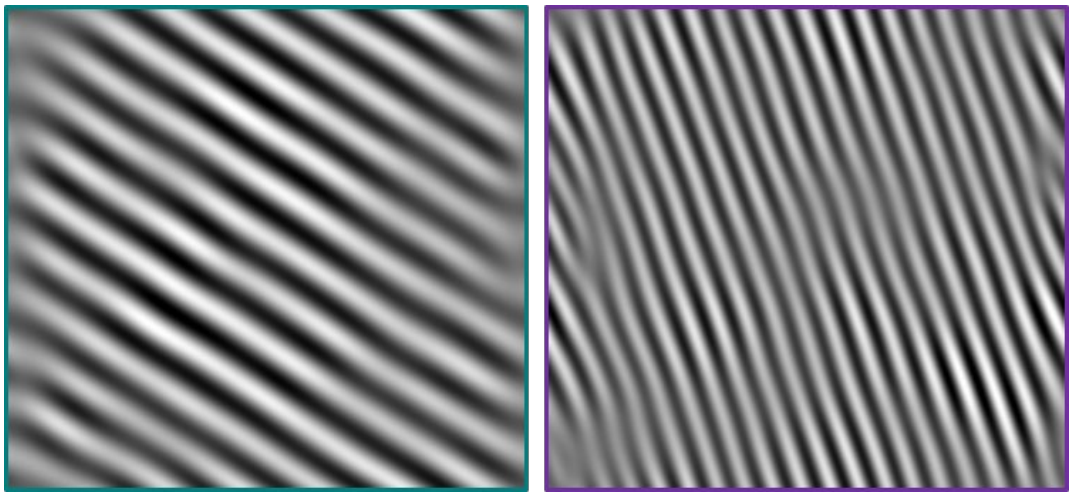

Fig. S10 The inverse fast Fourier transform(IFFT) of S-Fe/NIF sample based on different regions.

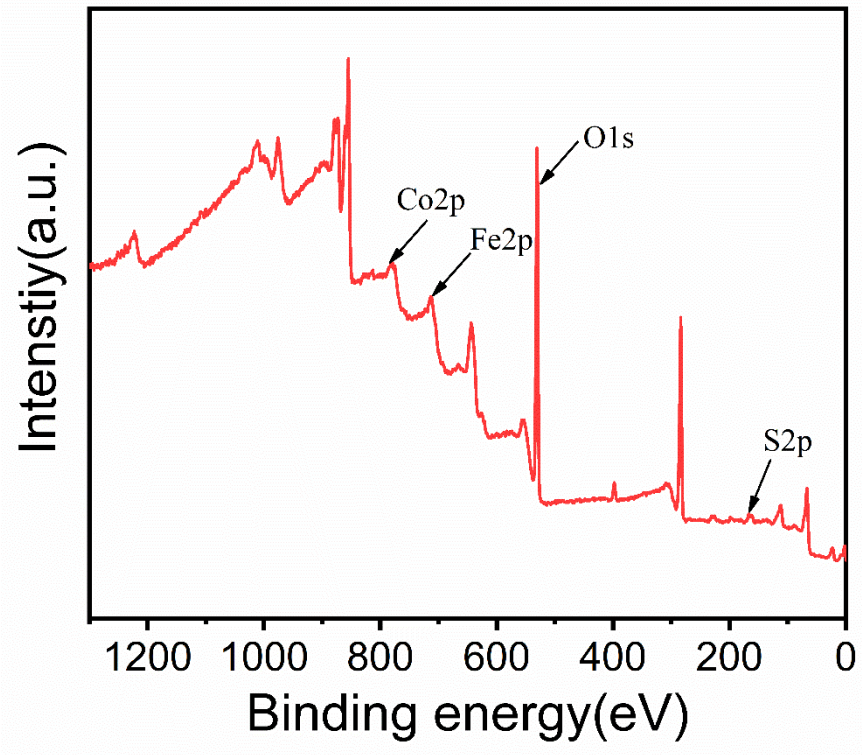

Fig. S11 The XPS spectrum of S-$FeCo_{1:1}$/NIF sample.

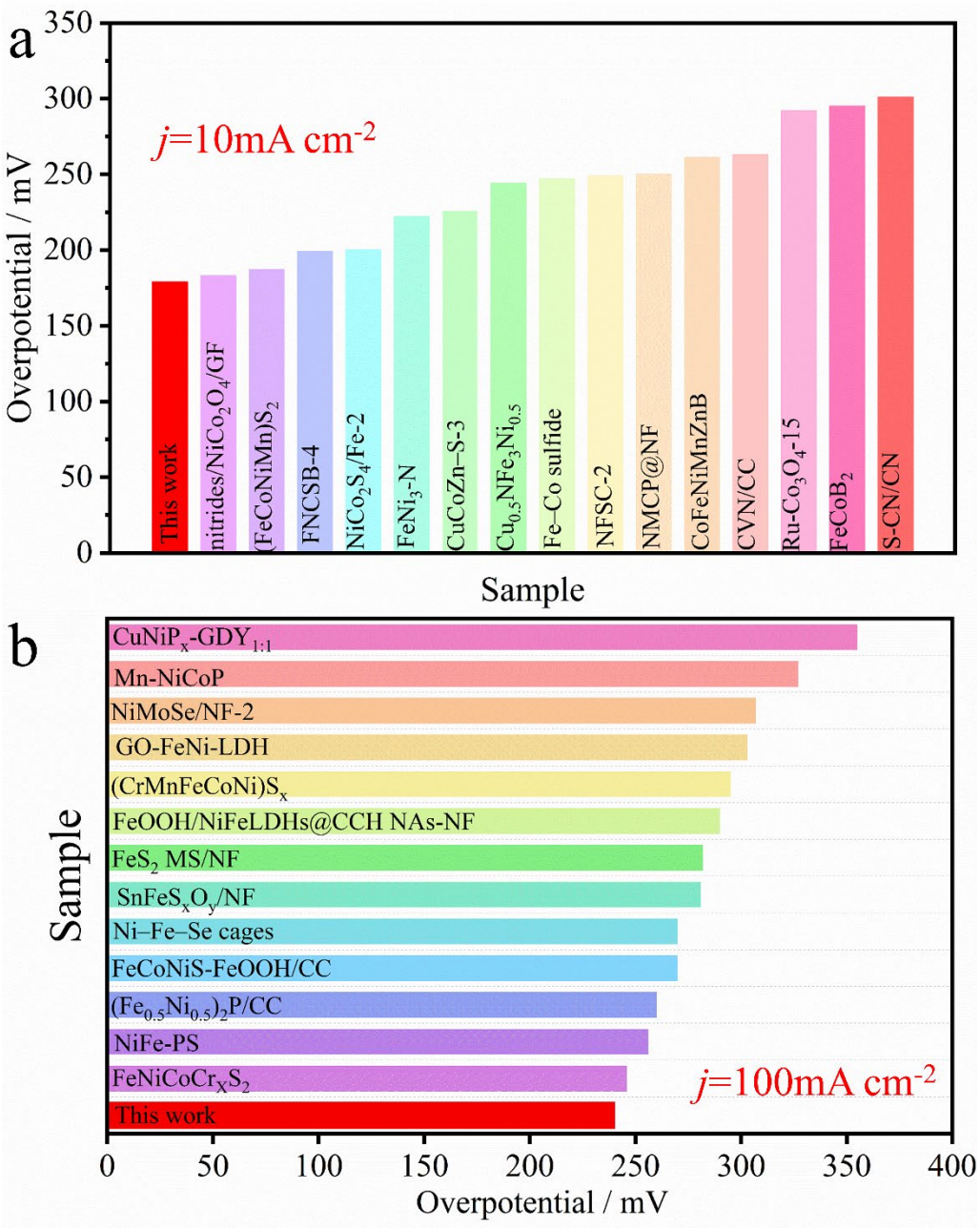

Fig. S12 The comparison of overpotentials of different catalysts of (a) 10 mA cm^{-2} and (b) 100 mA cm^{-2}.

Fig. S13 The electrochemical impedance spectroscopy equivalent circuit diagram.

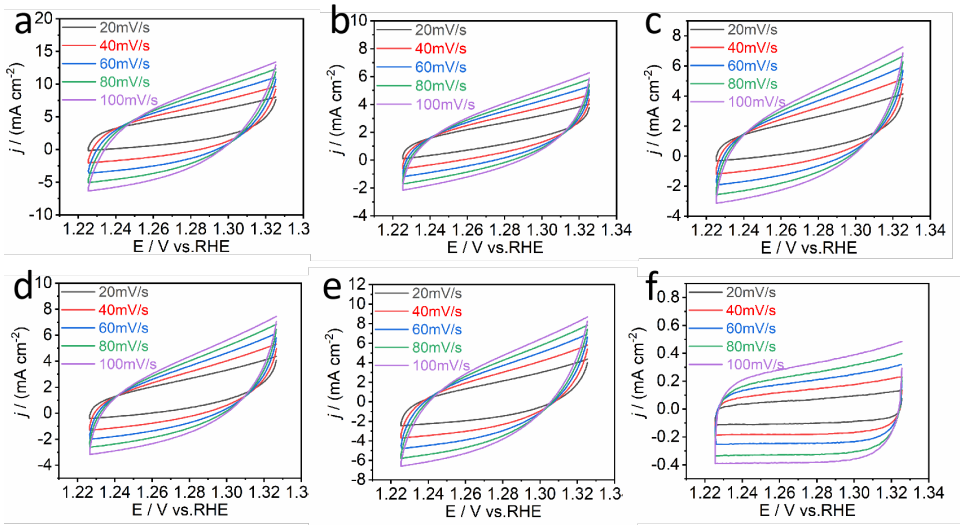

Fig. S14 CV curves of electrodes at different scan rates from 20 to 100 mV s^{-1}, (a) S-$FeCo_{1:1}$/NIF, (b) S-$FeCo_{2:1}$/NIF, (c) S-$FeCo_{1:2}$/NIF, (d) S-Fe/NIF, (e) S-Co/NIF and (f) NIF samples.

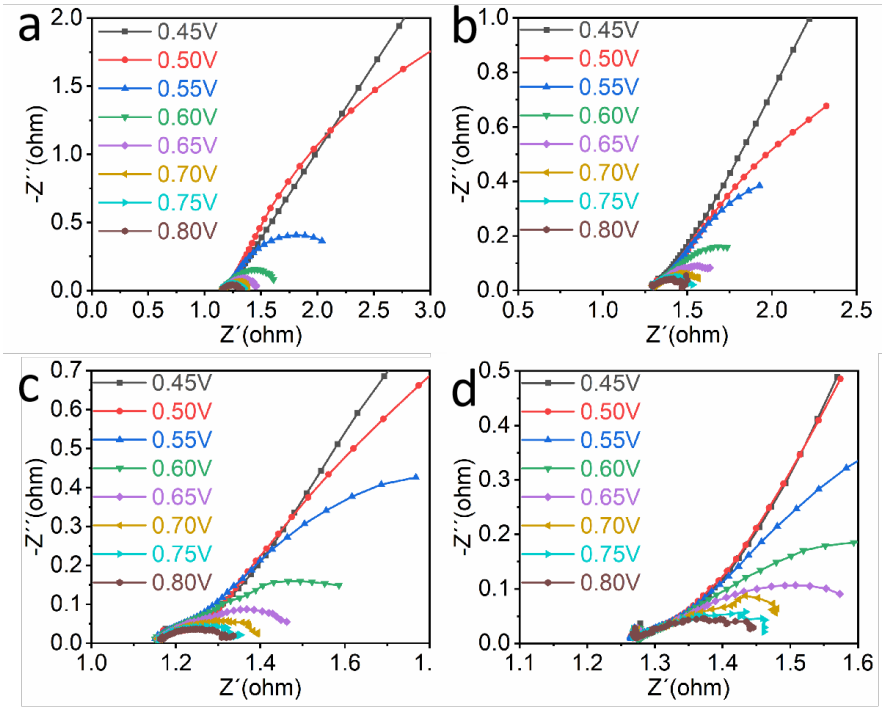

Fig. S15 The Operando Nyquist of (a) S-$FeCo_{2:1}$/NIF, (b) S-$FeCo_{1:2}$/NIF, (c) S-Fe/NIF, and (d) S-Co/NIF samples at various overpotentials in 1.0 M KOH electrolyte.

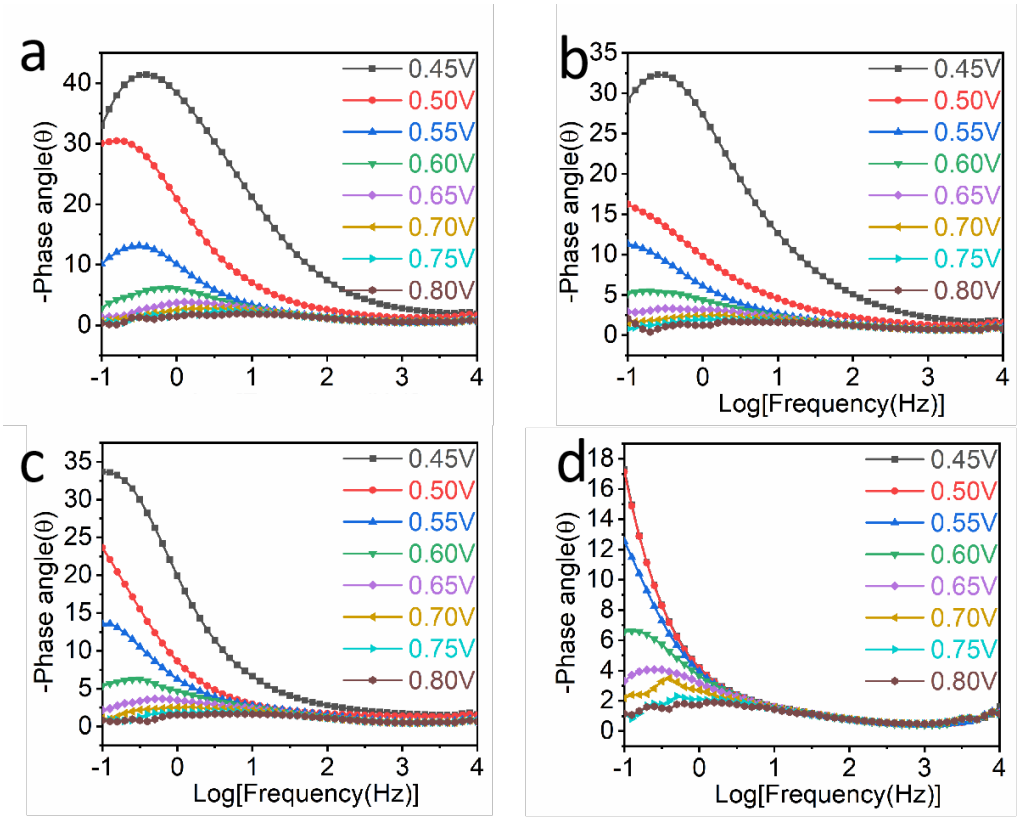

Fig. S16 The Bode phase plots of (a) S-FeCo$_{2:1}$/NIF, (b) S-FeCo$_{1:2}$/NIF, (c) S-Fe/NIF, and (d) S-Co/NIF samples at various overpotential in 1.0 M KOH electrolyte.

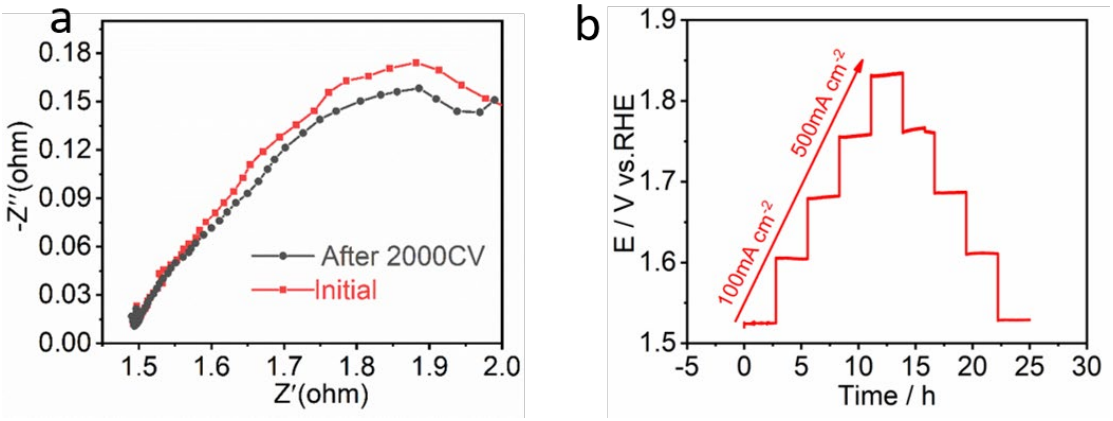

Fig. S17 (a) The electrochemical impedance spectroscopy of S-FeCo$_{1:1}$/NIF sample before and after the 2000 cycles. (b) The multi-current steps of S-FeCo$_{1:1}$/NIF sample.

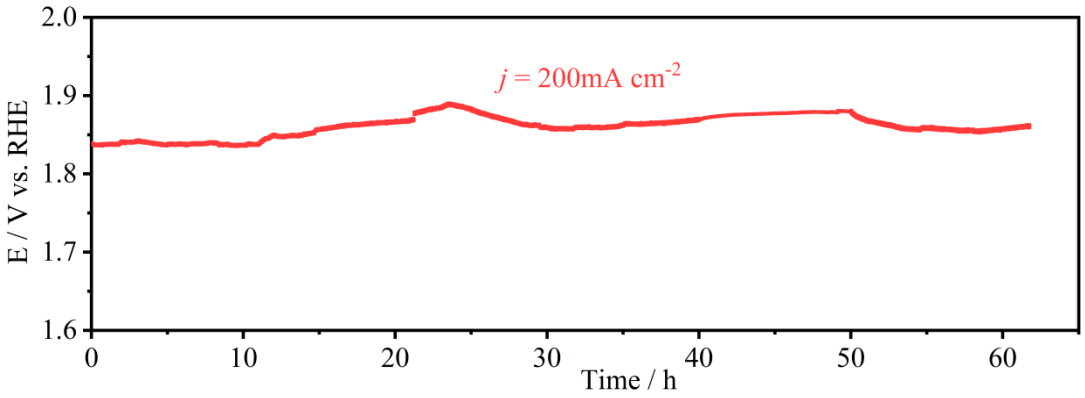

Fig. S18 The long-time E-t curves of S-Co/NIF for OER under a constant current of 200 mA cm^{-2}.

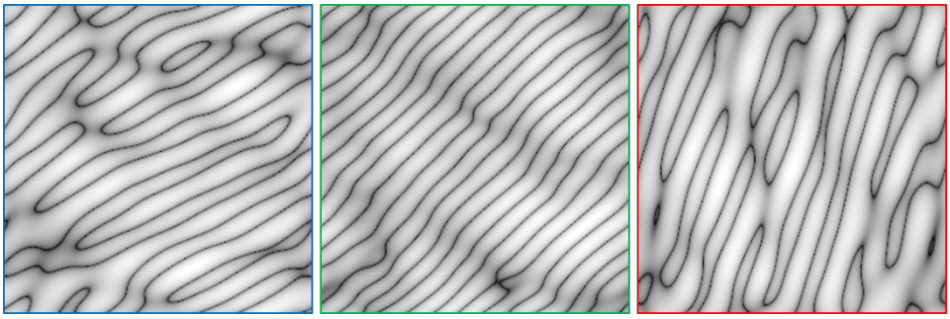

Fig. S19 The inverse fast Fourier transform(IFFT) of S-$FeCo_{1:1}$/NIF sample based on different regions of after OER.

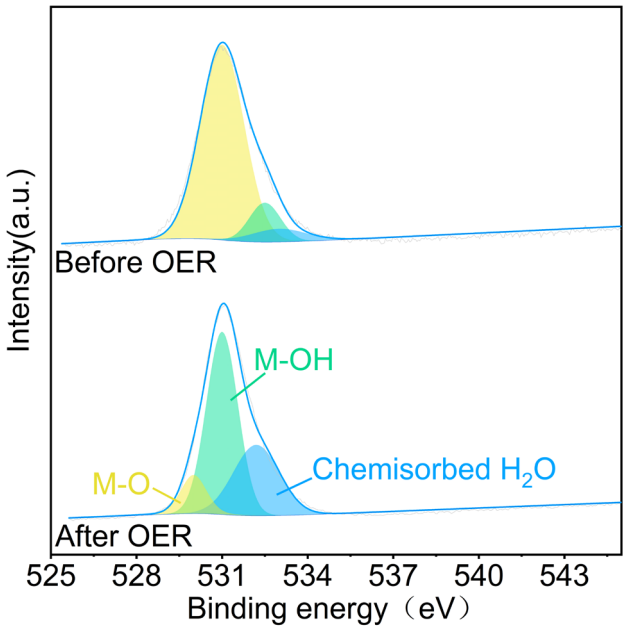

Fig. S20 The high-resolution O1s XPS spectra of S-$FeCo_{1:1}$/NIF sample before and after OER.

Fig. S21 Photograph of the *in situ* Raman testing setup. WE: working electrode, RE: reference electrode, and CE: counter electrode, respectively.

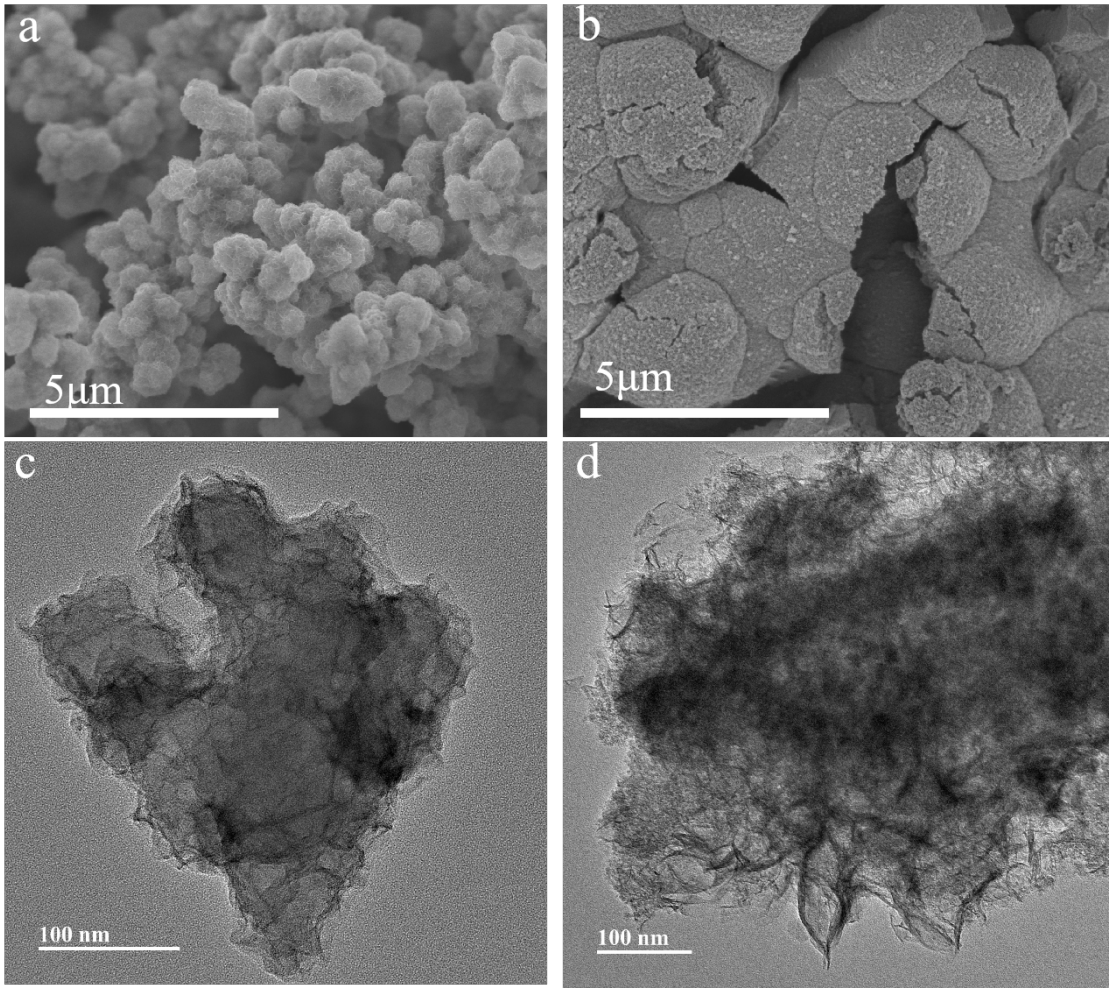

Fig. S22 The SEM images (a) before and (b) after OER and TEM images (c) before OER and (d) after OER of the S-Co/NIF sample.

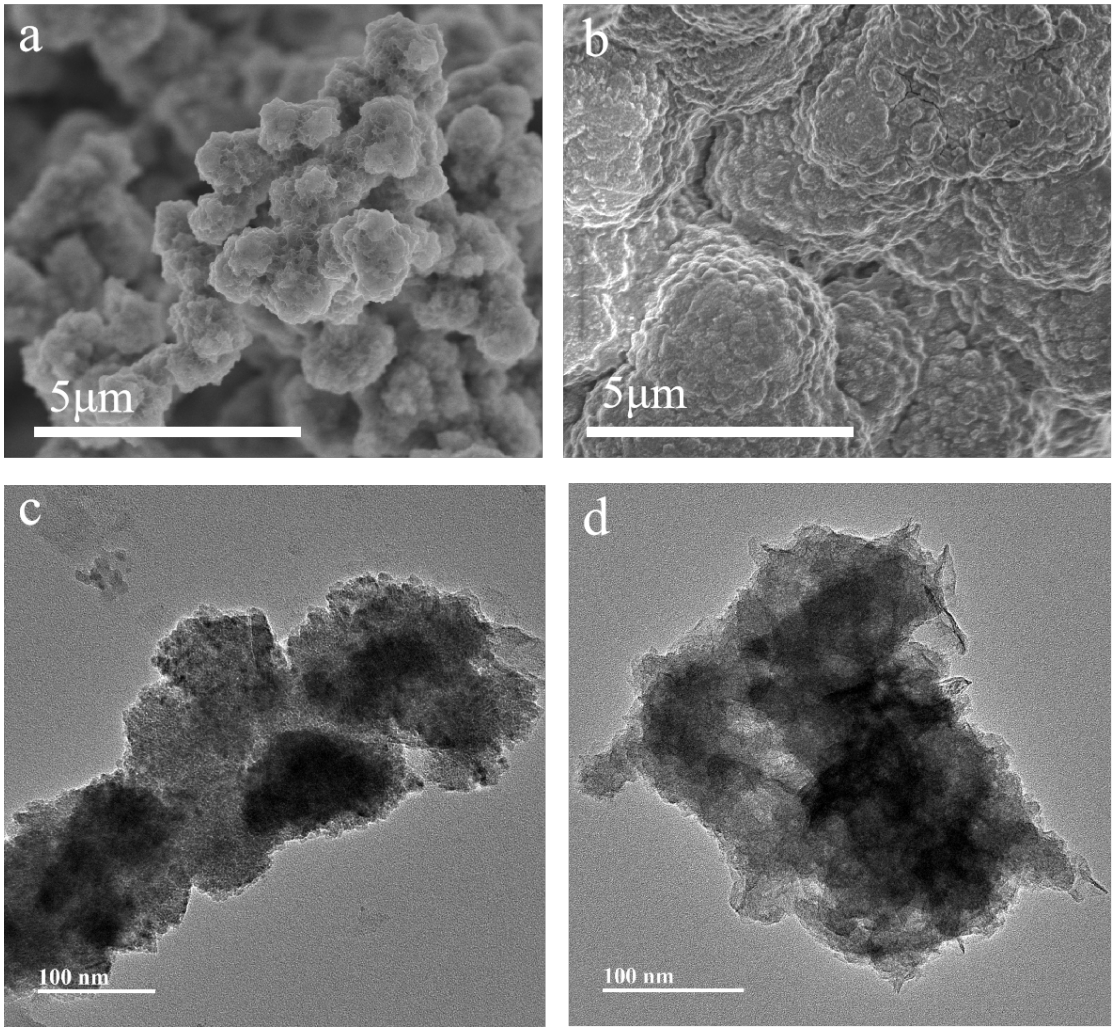

Fig. S23 The SEM images (a) before and (b) after OER and TEM images (c) before and (d) after OER of the S-Fe/NIF sample.

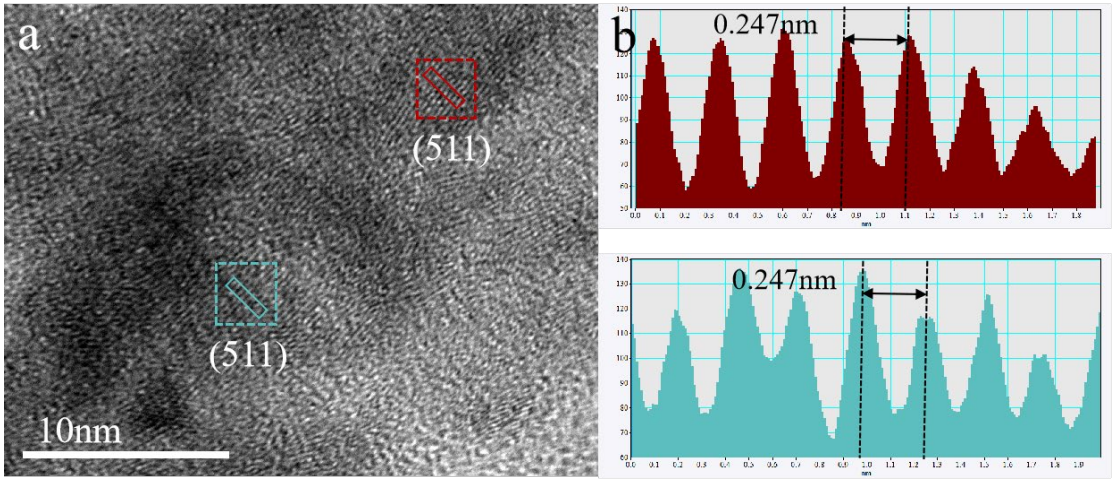

Fig. S24 The (a) HRTEM image and (b) corresponding intensity profiles along with the position of the S-Co/NIF sample.

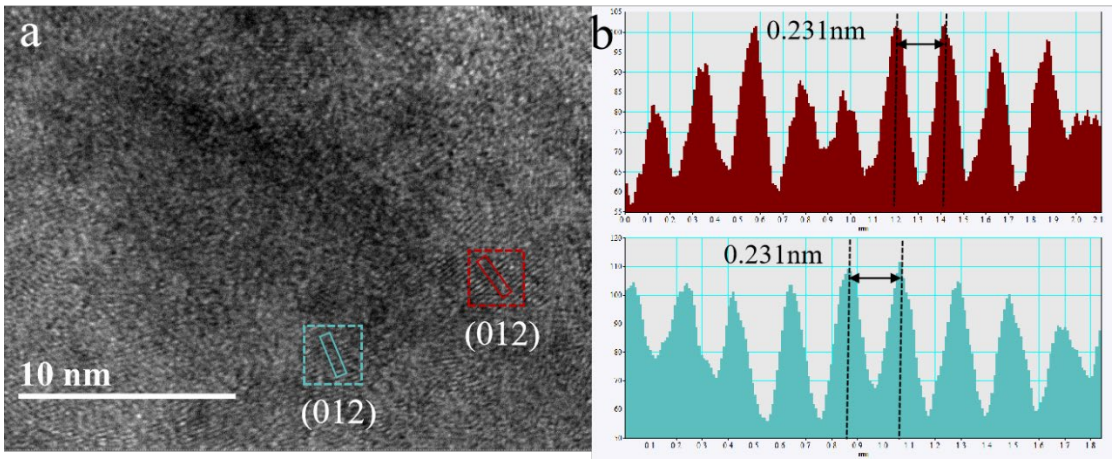

Fig. S25 The (a) HRTEM image and (b) corresponding intensity profiles along with the position of the S-Fe/NIF sample.

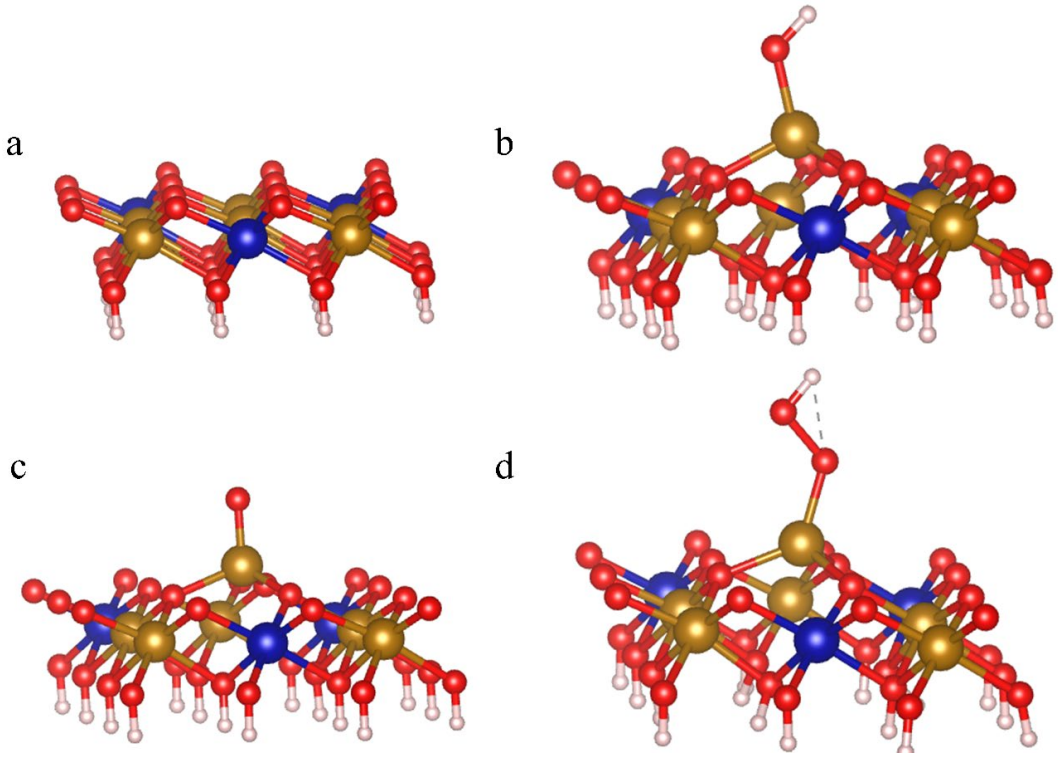

Fig. S26 Optimized configurations of (a) * and (b) *O, (c) *OH, and (d) *OOH species adsorbed on FeCoOOH-Fe model.

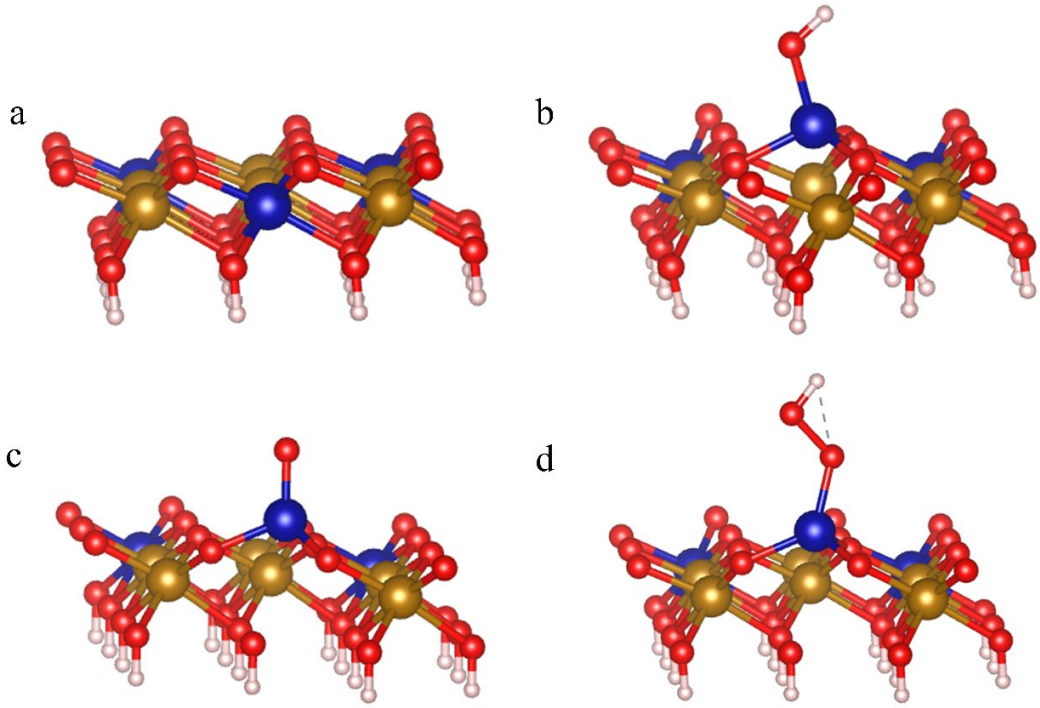

Fig. S27 Optimized configurations of (a) * and (b) *O, (c) *OH, and (d) *OOH species adsorbed on FeCoOOH-Co model.

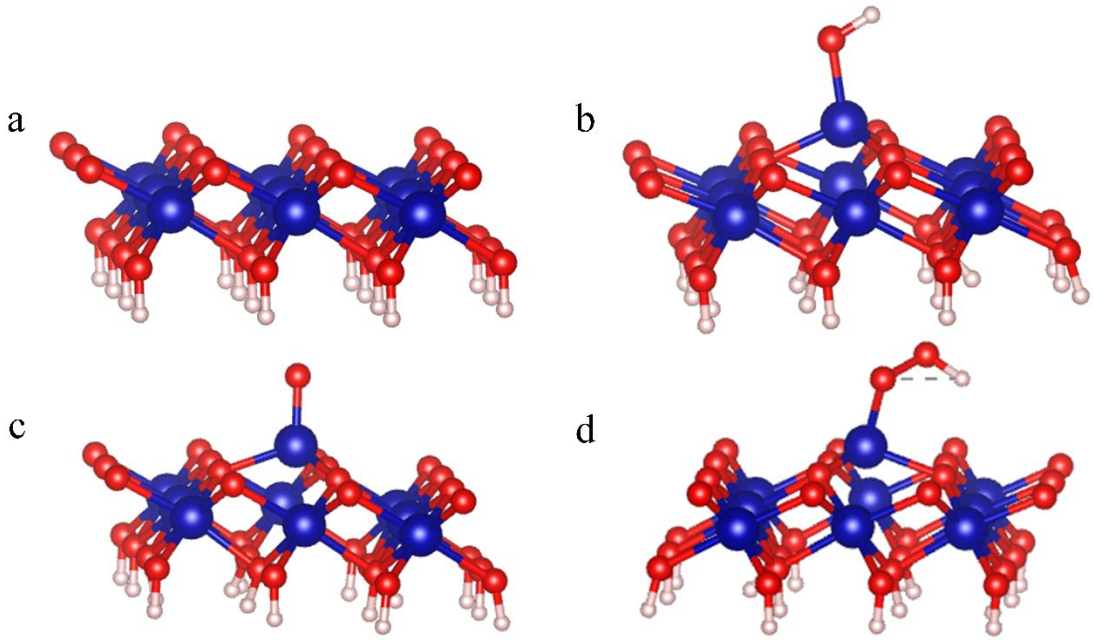

Fig. S28 Optimized configurations of (a) * and (b) *O, (c) *OH, and (d) *OOH species adsorbed on the CoOOH model.

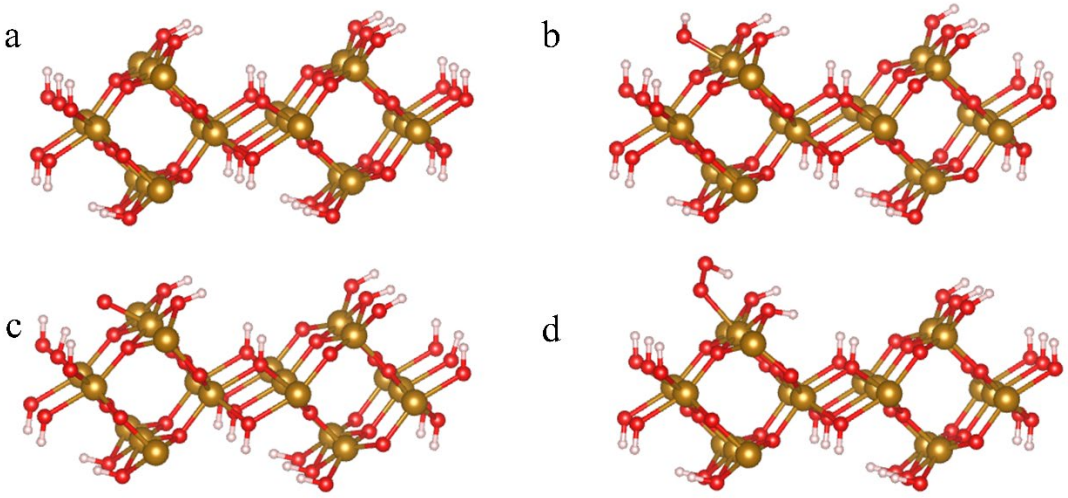

Fig. S29 Optimized configurations of (a) * and (b) *O, (c) *OH, and (d) *OOH species adsorbed on the FeOOH model.

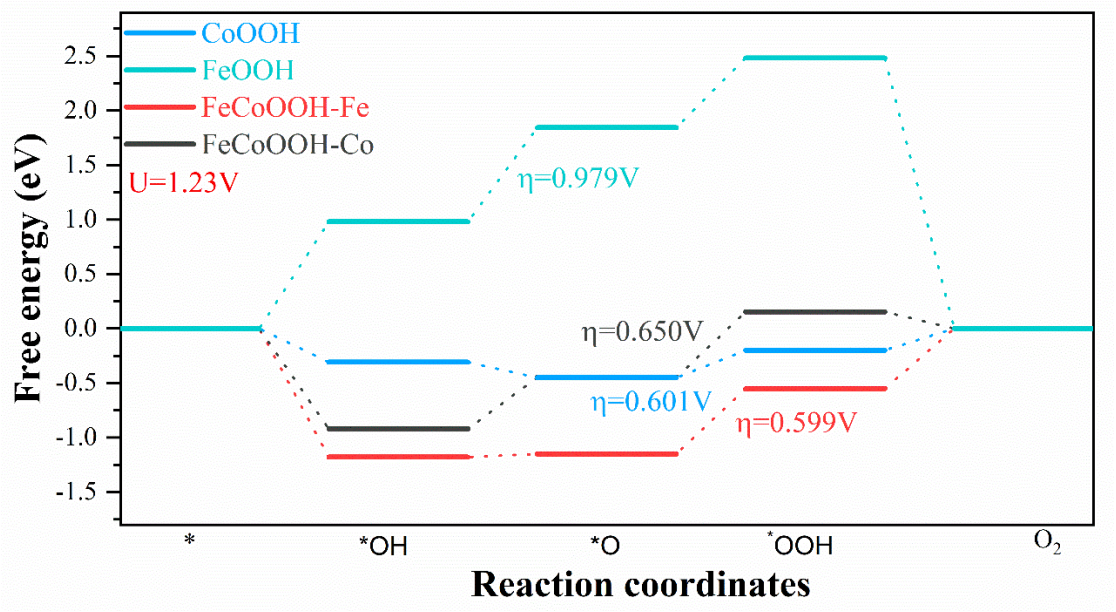

Fig. S30 The Gibbs free energy of different samples in each elementary step of OER at 1.23V.

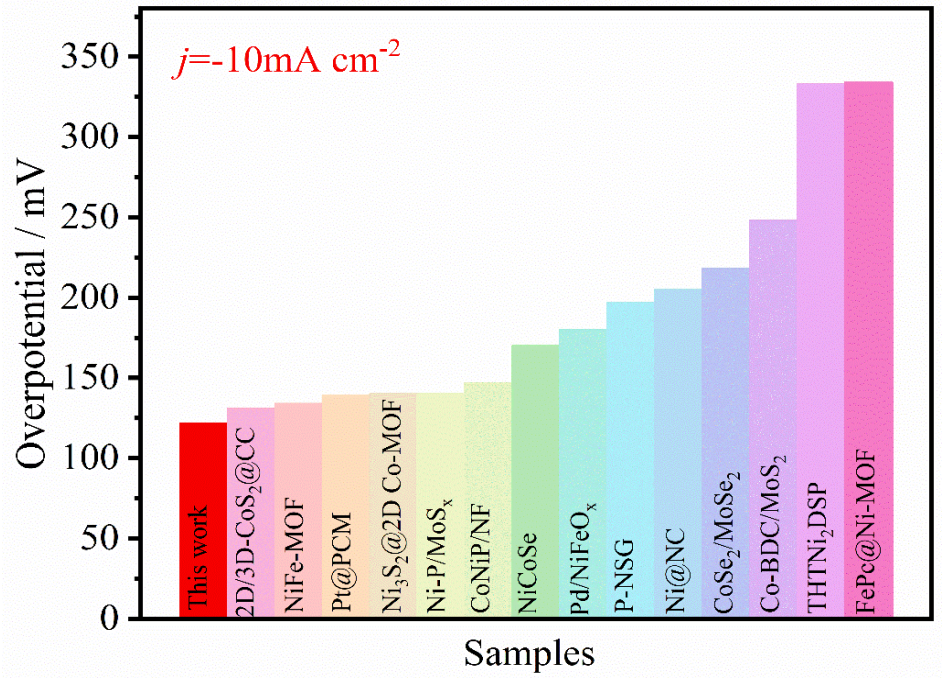

Fig. S31 Comparison of HER performance of different catalysts at 10 mA cm^{-2} .

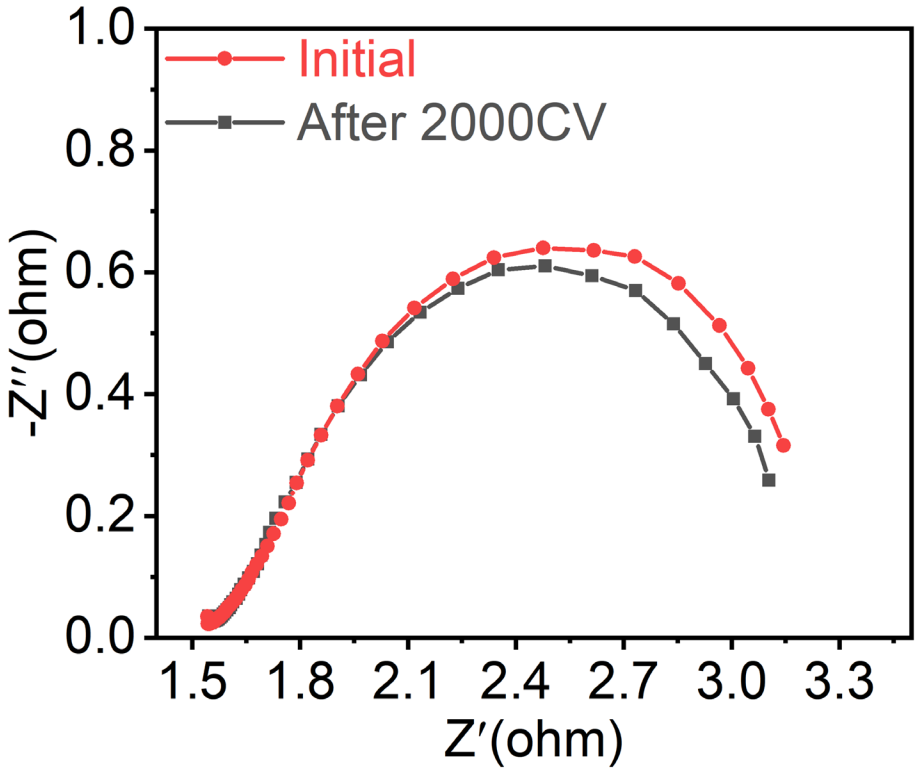

Fig. S32 The HER electrochemical impedance spectroscopy of S-FeCo$_{1:1}$/NIF electrode before and after 2000 cycles.

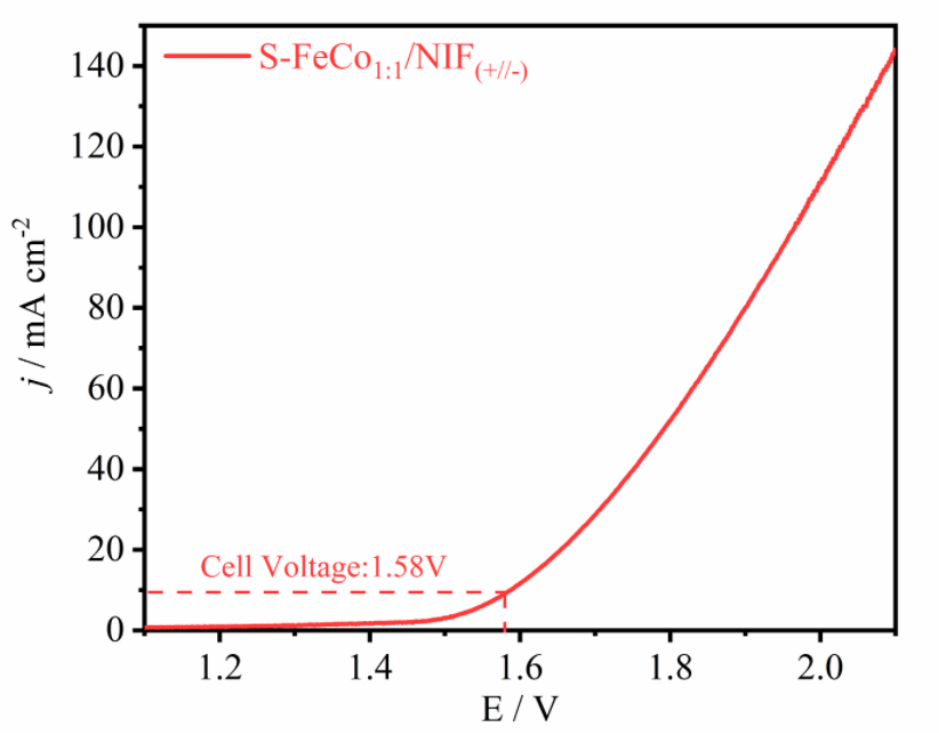

Fig. S33 The backsweep LSV plots of the S-FeCo$_{1:1}$/NIF||S-FeCo$_{1:1}$/NIF for overall alkaline water splitting.

3. Supplementary Tables

Table S1. ICP-AES analysis results of Co element in sample S-$FeCo_{1:1}$/NIF

Element label	Weight/g	Volume/ml	dilution coefficient	instrument reading /mg L^{-1}	sample concentration/mg kg^{-1}
Co	0.069	50	1	12.7899	9268.0645

Table S2. Comparison of the OER performance of S-$FeCo_{1:1}$/NIF catalyst with other reported OER catalysts.

Serial number	Catalyst	Overpotential / mV	Current density/mA cm^{-2}	Electrolyte	Reference
1	S-$FeCo_{1:1}$/NIF	179/240	10/100	1M KOH	This work
2	Mn-NiCoP	327	100	1M KOH	[2]
3	$SnFeS_xO_y$/NF	281	100	1M KOH	[3]
4	FeCoNiS-FeOOH/CC	270	100	1M KOH	[4]
5	$(CrMnFeCoNi)S_x$	295	100	1M KOH	[5]
6	$FeNiCoCrXS_2$	246	100	1M KOH	[6]
7	GO-FeNi-LDH	303	100	1M KOH	[7]
8	FeOOH/NiFeLDHs@CCH NAs-NF	290	100	1M KOH	[8]
9	NiFe-PS	256	100	1M KOH	[9]
10	CuNiPx-$GDY_{1:1}$	355	100	1M KOH	[10]
11	$(Fe_{0.5}Ni_{0.5})_2P$/CC	260	100	1M KOH	[11]
12	Ni–Fe–Se cages	270	100	1M KOH	[12]
13	NiMoSe/NF-2	307	100	1M KOH	[13]
14	CF-FeSO	230	100	1M KOH	[14]
15	$(FeCoNiMn_x)S_y$ MEMSs	232	100	1M KOH	[15]
16	FeS_2 MS/NF	282	100	1M KOH	[16]
17	CuCoZn–S-3	226	10	1M KOH	[17]
18	$NiCo_2S_4$/Fe-2	200	10	1M KOH	[18]
19	NFSC-2	249	10	1M KOH	[19]
20	$(FeCoNiMn)S_2$	187	10	1M KOH	[15]
21	Fe–Co sulfide	247	10	1M KOH	[20]
22	NMCP@NF	250	10	1M KOH	[21]
23	S-CN/CN	301	10	1M KOH	[22]
24	$FeNi_3$-N	222	10	1M KOH	[23]
25	$Cu_{0.5}NFe_3Ni_{0.5}$	244	10	1M KOH	[24]
26	CVN/CC	263	10	1M KOH	[25]
27	nitrides/$NiCo_2O_4$/GF	183	10	1M KOH	[26]
28	CoFeNiMnZnB	261	10	1M KOH	[27]
29	FNCSB-4	199	10	1M KOH	[28]
30	$FeCoB_2$	295	10	1M KOH	[29]
31	Ru-Co_3O_4-15	292	10	1M KOH	[30]

Table S3. The energy required for the active intermediates of different catalysts and the RDS table.

Sample	ΔG / eV	Overpotential / V	RDS
FeCoOOH-Fe			
OH-Fe	0.049528		
O-Fe	1.259978	0.029978	*O→*OOH
OOH-Fe	1.829244	0.599144	
Slab	1.78135	0.55135	
FeCoOOH-Co			
OH-Co	0.309711		
O-Co	1.701982	0.471982	*O→*OOH
OOH-Co	1.831935	0.601935	
Slab	1.076372	-0.153628	
CoOOH			
OH-Co	0.921409	-0.308591	
O-Co	1.087339	-0.142661	*O→*OOH
OOH-Co	1.880073	0.650073	
Slab	1.031179	-0.198821	
FeOOH			
OH-Fe	2.208889	0.978889	
O-Fe	2.095188	0.865188	*OH→*O
OOH-Fe	1.866509	0.636509	
Slab	-1.250586	0.471982	

Table S4. Comparison of the HER performance of S-$FeCo_{1:1}$/NIF catalyst with other reported HER catalysts.

Serial number	Catalyst	Overpotential / mV	Current density/mA cm^{-2}	Electrolyte	Reference
1	S-$FeCo_{1:1}$/NIF	122	10	1M KOH	This work
2	$THTNi_2DSP$	333	10	0.5M KOH	[31]
3	FePc@Ni-MOF	334	10	1M KOH	[32]
4	Ni@NC	205	10	1M KOH	[33]
5	NiCoSe	170	10	1M KOH	[34]
6	NiFe-MOF	134	10	1M KOH	[35]
7	Co-BDC/MoS_2	248	10	1M KOH	[36]
8	Ni_3S_2@2D Co-MOF/CP	140	10	1M KOH	[37]
9	CoNiP/NF	147	10	1M KOH	[38]
10	2D/3D-CoS_2@CC	131	10	1M KOH	[39]
11	$CoSe_2$/$MoSe_2$	218	10	1M KOH	[40]
12	Ni-P/MoS_x	140	10	1M KOH	[41]
13	Pt@PCM	139	10	1M KOH	[42]
14	Pd/$NiFeO_x$	180	10	1M KOH	[43]
15	P-NSG	197	10	1M KOH	[44]

Table S5. Comparison of the overall water splitting performance of S-$FeCo_{1:1}$/NIF catalyst with other reported bifunctional catalyst.

Serial number	Catalyst	potential / V	Current density/mA cm^{-2}	Electrolyte	Reference
1	S-FeCo1:1/NIF	1.58/1.81	10/50	1M KOH	This work
2	Cu_2S-Ni_3S_2	1.87	10	1M KOH	[45]
3	CuSe	1.68	10	1M KOH	[46]
4	Cu_3P nanobush	1.85	10	1M KOH	[47]
5	$CuCo_2O_4$	1.64	10	1M KOH	[48]
6	Ni_3S_2	1.66	10	1M KOH	[49]
7	$Ni_{11}(HPO_3)_8$ $(OH)_6$	1.60	10	1M KOH	[50]
8	Ni/$Mo_2C_{(1:2)}$-NCNFs	1.64	10	1M KOH	[51]
9	$Ni_{4.3}Co_{4.7}S_8$	1.63	10	1M KOH	[52]
10	Ni@NC	1.6	10	1M KOH	[33]

4. References

1. G. Kresse, J. Furthmüller, *Phy. Rev. B,* 1996, **54,** 11169-11186.
2. G. Ma, J. Ye, M. Qin, T. Sun, W. Tan, Z. Fan, L. Huang, X. Xin, *Nano Energy,* 2023, **115,** 108679.
3. T. Zhang, J. Han, T. Tang, J. Sun, J. Guan, *Int. J. Hydrogen Energy,* 2023, **48,** 4594-4602.
4. W. Teng, M. Huo, Z. Sun, W. Yang, X. Zheng, C. Ding, S. Zhang, *Front. Chem.,* 2020, **8**.
5. M. Cui, C. Yang, B. Li, Q. Dong, M. Wu, S. Hwang, H. Xie, X. Wang, G. Wang, L. Hu, *Adv. Energy Mater.,* 2021, **11,** 2002887.
6. T. X. Nguyen, Y.-H. Su, C.-C. Lin, J.-M. Ting, *Adv. Funct. Mater.,* 2021, **31,** 2106229.
7. X. Han, N. Suo, C. Chen, Z. Lin, Z. Dou, X. He, L. Cui, *Int. J. Hydrogen Energy,* 2019, **44,** 29876-29888.
8. J. Chi, H. Yu, G. Jiang, J. Jia, B. Qin, B. Yi, Z. Shao, *J.Mater. Chem.A,* 2018, **6,** 3397-3401.
9. J. Zhang, H. Yu, J. Yang, X. Zhu, M. Hu, J. Yang, *J. Alloys Compd.,* 2022, **924,** 166613.
10. J. Gao, Y. Li, X. Yu, Y. Ma, *J. Colloid Interface Sci.,* 2022, **628,** 508-518.
11. D. Wu, A. Kong, W. Li, Y. Fu, J. Zhang, *Int. J. Hydrogen Energy,* 2021, **46,** 39844-39854.
12. J. Nai, Y. Lu, L. Yu, X. Wang, X. W. Lou, *Small,* 2017, **29,** 1703870.
13. W. Feng, M. Bu, S. Kan, X. Gao, A. Guo, H. Liu, L. Deng, W. Chen, *Appl. Mater. Today,* 2021, **25,** 101175.
14. W. H. Lee, M. H. Han, Y.-J. Ko, B. K. Min, K. H. Chae, H.-S. Oh, *Nat. Commun.,* 2022, **13,** 605.
15. F. Li, H. Wu, S. Lv, Y. Ma, B. Wang, Y. Ren, C. Wang, Y. Shi, H. Ji, J. Gu, S. Tang, X. Meng, *Small,* 2309025.
16. C. Yue, X. Zhang, J. Yin, H. Zhou, K. Liu, X. Liu, *Appl. Catal. B,* 2023, **339,** 123171.
17. J. Bai, N. Lei, L. Wang, Y. Gong, *Nanoscale,* 2022, **14,** 17976-17984.
18. X. Li, Z. Kou, S. Xi, W. Zang, T. Yang, L. Zhang, J. Wang, *Nano Energy,* 2020, **78,** 105230.
19. F. Xiao, P. He, P. Yang, R. Su, Y. Wang, M. Zhao, B. Jia, *J. Alloys Compd.,* 2023, **938,** 168573.
20. Y. Liu, X. Xie, G. Zhu, Y. Mao, Y. Yu, S. Ju, X. Shen, H. Pang, *J. Mater. Chem. A,* 2019, **7,** 15851-15861.
21. M. R. Kandel, U. N. Pan, D. R. Paudel, P. P. Dhakal, N. H. Kim, J. H. Lee, *Compos.B. Eng.,* 2022, **239,** 109992.
22. H.-W. Zhang, Y.-X. Lu, B. Li, G.-F. Huang, F. Zeng, Y.-Y. Li, A. Pan, Y.-F. Chai, W.-Q. Huang, *J. Mater. Sci.Technol.,* 2021, **86,** 210-218.
23. Q. Chen, N. Gong, T. Zhu, C. Yang, W. Peng, Y. Li, F. Zhang, X. Fan, *Small* 2022, **18,** 2105696.
24. H. Tang, D. Yang, M. Lu, S. Kong, Y. Hou, D. Liu, D. Liu, S. Yan, Z. Chen, T. Yu, Z. Zou, *J. Mater. Chem. A,* 2021, **9,** 25435-25444.
25. S. Dutta, A. Indra, Y. Feng, H. Han, T. Song, *Appl. Catal. B,* 2019, **241,** 521-527.
26. Z. Liu, H. Tan, D. Liu, X. Liu, J. Xin, J. Xie, M. Zhao, L. Song, L. Dai, H. Liu, *Adv. Sci,* 2019, **6,** 1801829.
27. X. Wang, Y. Zuo, S. Horta, R. He, L. Yang, A. Ostovari Moghaddam, M. Ibáñez, X. Qi, A. Cabot, *ACS Appl.Mater. Inter.,* 2022, **14,** 48212-48219.
28. Z. Chen, R. Zheng, W. Zou, W. Wei, J. Li, W. Wei, B.-J. Ni, H. Chen, *Appl. Catal. B,* 2021,

298, 120583.
29. X. Zou, W. Zhang, X. Zhou, K. Song, X. Ge, W. Zheng, *J. Energy Chem.,* 2022, **72,** 509-515.
30. R. Madhu, A. Karmakar, P. Arunachalam, J. Muthukumar, P. Gudlur, S. Kundu, *J. Mater. Chem. A,* 2023, **11,** 21767-21779.
31. R. Dong, M. Pfeffermann, H. Liang, Z. Zheng, X. Zhu, J. Zhang, X. Feng, *Angew. Chem. Int. Ed.,* 2015, **54,** 12058-12063.
32. X. Zhang, R. Lin, X. Meng, W. Li, F. Chen, J. Hou, *Inorg. Chem.,* 2021, **60,** 9987-9995.
33. Y. Xu, W. Tu, B. Zhang, S. Yin, Y. Huang, M. Kraft, R. Xu, *Adv. Mater.,* 2017, **29,** 1605957.
34. Y. Zhou, Y. Chen, M. Wei, H. Fan, X. Liu, Q. Liu, Y. Liu, J. Cao, L. Yang, *CrystEngComm,* 2021, **23,** 69-81.
35. J. Duan, S. Chen, C. Zhao, *Nat. Commun.,* 2017, **8,** 15341.
36. D. Zhu, J. Liu, Y. Zhao, Y. Zheng, S.-Z. Qiao, *Small,* 2019, **15,** 1805511.
37. J. Cheng, X. Yang, X. Yang, R. Xia, Y. Xu, W. Sun, J. Zhou, *Fuel Process. Technol.,* 2022, **229,** 107174.
38. H. Liu, R. Huang, W. Chen, Y. Zhang, M. Wang, Y. Hu, Y. Zhou, Y. Song, *Appl. Surf. Sci.,* 2021, **569,** 150762.
39. Z. Fu, D. Wang, Z. Xu, L. Zeng, W. Geng, *Electrocatalysis,* 2022, **13,** 306-316.
40. G. Zhao, P. Li, K. Rui, Y. Chen, S. X. Dou, W. Sun, *Chem. Eur. J.,* 2018, **24,** 11158-11165.
41. G.-Q. Han, X. Li, J. Xue, B. Dong, X. Shang, W.-H. Hu, Y.-R. Liu, J.-Q. Chi, K.-L. Yan, Y.-M. Chai, C.-G. Liu, *Int. J. Hydrogen Energy,* 2017, **42,** 2952-2960.
42. H. Zhang, P. An, W. Zhou, B. Y. Guan, P. Zhang, J. Dong, X. W. Lou, *Sci. Adv,* 2018, **4,** eaao6657.
43. W. Zhang, X. Jiang, Z. Dong, J. Wang, N. Zhang, J. Liu, G.-R. Xu, L. Wang, *Adv. Funct. Mater.,* 2021, **31,** 2107181.
44. Y. Tian, R. Mei, D.-z. Xue, X. Zhang, W. Peng, *Electrochim. Acta,* 2016, **219,** 781-789.
45. K. S. Bhat, H. S. Nagaraja, *ChemistrySelect,* 2020, **5,** 2455-2464.
46. B. Chakraborty, R. Beltrán-Suito, V. Hlukhyy, J. Schmidt, P. W. Menezes, M. Driess, *ChemSusChem,* 2020, **13,** 3222-3229.
47. S. Wei, K. Qi, Z. Jin, J. Cao, W. Zheng, H. Chen, X. Cui, *ACS Omega,* 2016, **1,** 1367-1373.
48. A. T. Aqueel Ahmed, S. M. Pawar, A. I. Inamdar, H. Kim, H. Im, *Adv. Mater. Inter.,* 2020, **7,** 1901515.
49. X. Ma, W. Zhang, Y. Deng, C. Zhong, W. Hu, X. Han, *Nanoscale,* 2018, **10,** 4816-4824.
50. P. W. Menezes, C. Panda, S. Loos, F. Bunschei-Bruns, C. Walter, M. Schwarze, X. Deng, H. Dau, M. Driess, *Energy & Environ.Sci.,* 2018, **11,** 1287-1298.
51. M. Li, Y. Zhu, H. Wang, C. Wang, N. Pinna, X. Lu, *Adv. Energy Mater.,* 2019, **9,** 1803185.
52. Y. Tang, H. Yang, J. Sun, M. Xia, W. Guo, L. Yu, J. Yan, J. Zheng, L. Chang, F. Gao, *Nanoscale,* 2018, **10,** 10459-10466.